Earth Planets Space, **58**, 633–643, 2006

A study of the storm event on October 21–22, 1999 by the MHD simulation

K. S. Park and T. Ogino

Solar-Terrestrial Environment Laboratory, Nagoya University, Japan

(Received May 18, 2005; Revised January 14, 2006; Accepted January 16, 2006; Online published May 12, 2006)

We carried out a high resolution three-dimensional magnetohydrodynamic (MHD) simulation of the interaction between the solar wind and the Earth's magnetosphere during a strong magnetic storm on October 21–22, 1999. The input to the simulation was from WIND solar wind observations. As the IMF is strongly southward (-20 nT to -30 nT) for 6 hours, the geomagnetic field lines in the dayside magnetopause are eroded to the geosynchronous orbit (GEO) region by reconnection. The associated magnetic flux is transferred from the dayside magnetosphere to the tail. The reconnection region still appears near GEO region on the dayside magnetopause, even though the IMF B_z component becomes small or northward, because of the influence of the strong IMF B_y (30 nT). IMF lines can successively reconnect with the naked and large geomagnetic field line in the dayside flank regions. Thus, the cross polar cap potential is maintained to be large value and convection in the ionosphere is enhanced. The cross polar cap potential is governed by IMF B_y as well as B_z ($\phi \sim 250$ kV for $B_z \sim -20$ nT and $\phi \sim 300$ kV for $B_z \sim -30$ nT), and it saturates during the strong southward IMF. A large energy flux enters the ionosphere at very low latitudes (50°) and the inner edge of the plasma sheet becomes very close to the Earth ($X = -3.2\ R_E$) for a strong magnetic storms. The open-closed boundary extends to 60° latitudes on the nightside, 72° on the dayside, 62° on dawn, and 66° on dusk. Enhanced energy flux appears at low latitudes (50°) on the nightside in simulation. Moreover, the energy flux in the dusk region (19 MLT) appears down to 55° latitude in simulation, which is consistent with the low latitude boundary of the 0.02–20 keV particles detected by TED of the NOAA-15. A convective electric field, which is penetrating to the Earth-side of the NENL, is almost comparable to that of the solar wind. The present MHD simulation study give reasonable results even for extreme conditions and thereby its usefulness is demonstrated as a physical model for space weather studies.
Key words: A global MHD simulation, storm event study.

1. Introduction

Early simulations of the interaction between the solar wind and the magnetosphere (Lyon *et al.*, 1981; Brecht *et al.*, 1981; Ogino *et al.*, 1985; Walker *et al.*, 1993) were applied to ideal cases in which the solar wind and the interplanetary magnetic field (IMF) were constant.

In recent years, global MHD simulations have been used to model magnetospheric events by using actual solar wind observations as input. One of the first of these global MHD simulations was carried out by using the solar wind data for a 1-hour period on October 19, 1986 (Fedder *et al.*, 1995). The solar wind velocity was high and almost constant with 660 km/s and IMF B_y and B_z were about -6 nT and -6 nT, respectively, in that event. They showed that closed field lines in the northern dusk region extended to higher latitudes due to the negative IMF B_y. In order to develop a Global Geospace Circulation Model (GGCM), MHD simulations were run for two time intervals on January 27, 1992 (1325–1715 UT and 1730–1930 UT) and were compared with observations (Raeder *et al.*, 1998; Lyons, 1998). The IMF was northward on average, with a large B_y component ($B_y = -20$ nT), and the dynamic pressure (Dp ~ 4 nPa) was about 2 to 3 times larger than normal. They found a good qualitative agreement between the simulated potential patterns and those from the Assimilative Mapping of Ionospheric Electrodynamics (AMIE) empirical model.

Raeder *et al.* (2001) used a global model of Earth's magnetosphere and ionosphere to simulate the Geospace Environment Modeling (GEM) substorm challenge event on November 24, 1996, and the simulation of a substorm timing was also studied by Slinker *et al.* (2001), Lyons *et al.* (2001) and Ashour-Abdalla *et al.* (2002b). In this event, northward IMF ($\sim +5$ nT) for ~ 80 min, followed by a sudden rotation of the IMFsouthward (~ -7 nT). The GEM substorm challenge event provided them with a unique opportunity to compare their model with observation and to assess its validity with respect to substorm dynamics. Ashour-Abdalla *et al.* (1999, 2002a) investigated a substorm during a very active period on December 22, 1996 and found a good agreement between the onset time of the substorm in their global MHD simulation and that inferred from Polar observation images. Le *et al.* (2001) used a simulation and data to investigate magnetospheric dynamics during an extended period of strongly northward IMF (20 nT) on April 11, 1997. They found that the location of the reconnection layer was in agreement with the Polar observations but the layer was much thinner than that predicted by the MHD simulation. Global MHD simulations have been quite successful in reproducing overall magnetospheric dynamics. They usually reproduce the time changes

that occur in the auroral ionosphere. However, there are a few simulations with a high spatial resolution to quantitatively study the effects of a long time duration of strong southward IMF for magnetic storms. How much energy are transported from the solar wind through the magnetosphere into the ionosphere during such an extreme condition, and how is it transported? We also need to understand the magnetospheric phenomena such as the dayside reconnection and potential saturation by the effects of large IMF B_z and B_y component.

In this paper, we present the results of a strong magnetic storm event study by using a three-dimensional global MHD model during which the IMF was strongly southward for a long time. We chose an event on October 22, 1999 during which strong auroral electrojet and ring current disturbances were observed. The dynamic pressure of solar wind varied from 1.8 to 51.8 nPa and the IMF B_z was about -31 nT for three hours. The Kp index was 8- during this period and Dst reached -237 nT. In Section 2, we describe the MHD simulation model. In Section 3, we explain characteristic features of the events observations on October 22. Simulation results are presented in Section 4 and the chronology of simulated substorms are explained in Section 5. We discuss the results in comparison with observations in Section 6. Finally, conclusions are summarized in Section 7.

2. Simulation Model

2.1 Basic Equations

We have solved the normalized resistive MHD and Maxwell's equations as an initial value problem by using a modified version of the Leap-Frog scheme. The basic MHD simulation model has been described in detail by Ogino *et al*. (1992). The normalized MHD equations are written as follows:

$$\frac{\partial \rho}{\partial t} = -\nabla \cdot (\mathbf{V}\rho) + D\nabla^2 \rho, \tag{1}$$

$$\frac{\partial \mathbf{V}}{\partial t} = -(\mathbf{V}\cdot\nabla)\mathbf{V} - \frac{1}{\rho}\nabla P + \frac{1}{\rho}\mathbf{J}\times\mathbf{B} + \mathbf{g} + \frac{1}{\rho}\mu\nabla^{\mathbf{2}}\mathbf{V}, \tag{2}$$

$$\frac{\partial P}{\partial t} = -(\mathbf{V}\cdot\nabla)P - \gamma P\nabla\cdot\mathbf{V} + D_p\nabla^{\mathbf{2}}P, \tag{3}$$

$$\frac{\partial \mathbf{B}}{\partial t} = \nabla\times(\mathbf{V}\times\mathbf{B}) + \eta\nabla^{\mathbf{2}}\mathbf{B}, \tag{4}$$

$$\mathbf{J} = \nabla\times(\mathbf{B} - \mathbf{B_d}) \tag{5}$$

where ρ is the plasma density, $\mathbf{V}$ is the plasma flow velocity, P is the plasma pressure, $\mathbf{B}$ is the magnetic field, $\mathbf{B_d}$ is the dipole field of Earth, $\mathbf{J}$ is the current density, $\mathbf{g} = -g_0/\xi^3$ ($\xi^2 = x^2 + y^2 + z^2$, $g_0 = 1.35\times10^{-6}$ (9.8 m/s^2)) is the force of gravity, $\mu\nabla^2\mathbf{V}$ is the viscosity, and γ is the ratio of specific heats; $\gamma = 5/3$. $\eta = \eta_0(T/T_0)^{-3/2}$ is the resistivity, where $T = P/\rho$ is the temperature, and T_0 is the ionospheric temperature. The model resistivity η_0 is set to 0.001 and the diffusion coefficient is $D = D_p = \mu_0 = \mu/\rho_{sw} = 0.001$, where ρ_{sw} is the solar wind plasma density. The magnetic Reynolds number is $S = \tau_\eta/\tau_A$ = 100–2000 where $\tau_\eta \equiv \Delta x^2/\eta$, $\tau_A = \Delta x/V_A$, and Δx is the mesh size. The normalized quantities in the basic equations are the radius of the Earth, $R_E = 6.37\times10^6$ m, the Alfvén transit time, $\tau_A = R_E/v_A = 0.937$ s, the density at the ionosphere, $\rho_s = mn_s$ ($n_s = 10^{10}$ m^{-3}), the magnetic field at one Earth radius at the equator, $B_s = 3.12\times10^{-5}$ T, and the Alfvén velocity at the surface of the Earth, $v_A = B_s/(\mu_0\rho_s)^{1/2} = 6.80\times10^6$ m/s.

2.2 Boundary Conditions

We use a simulation box with dimensions of $X_1 \le X \le X_0$, $0 \le Y \le Y_0$, $Z_1 \le Z \le Z_0$, in Cartesian solar-magnetospheric coordinates. For this simulation the boundaries are $X_0 = 30\ R_E$, $X_1 = -120\ R_E$, $Y_0 = 60\ R_E$, and $-Z_1 = Z_0 = 60\ R_E$. A mirror dipole field is applied in the solar wind at time t = 0 to take up the shape of the magnetopause. Watanabe and Sato (1990) have shown that this initial condition helps assure that $\nabla\cdot\mathbf{B} = 0$ throughout the simulation box. The Earth is located at the origin of the simulation box, $\mathbf{r} = (X, Y, Z) = (0\ R_E, 0\ R_E, 0\ R_E)$ and the solar wind flows into the box in the X-direction through the upstream boundary at $X = X_0$. The number of grid points is $(n_X, n_Y, n_Z) = (500, 200, 400)$ with a uniform grid spacing of $\Delta X = 0.3\ R_E$. The following boundary conditions are imposed for each physical quantity, $\phi = (\rho, \mathbf{V}, P, \mathbf{B})$. At the upstream boundary for $X = X_0$, we use 1 minute solar wind data acquired by the WIND satellite as input parameters (ρ, V_x, P, B_y, B_z) of the simulation. The IMF B_x component is not used to keep a layered structure of the IMF lines in the solar wind. The WIND parameters are sampled at different times so we used linear interpolation to calculate all of the parameters at the same time.

The simulation quantities are connected with the solar wind quantity at each proper time step ($32\Delta\ t$) by introduction of a smooth function, where Δt is a time step. The internal quantity, $\phi_{\rm in}$, at the initial state in the ionosphere and the external quantity of the simulated parameter, $\phi_{\rm ex}$, are connected at each time step by the introduction of a smooth function, f

$$\phi = f\phi_{\rm ex} + (1 - f)\phi_{\rm in},$$

where $f \equiv a_0h^2/(a_0h^2+1)$, $a_0 = 100$, $h = (\xi/\xi_a)^2 - 1$ for $\xi \ge \xi_a$, and $h = 0$ for $\xi < \xi_a$. The smooth function damps out all perturbations near the ionosphere including parallel currents. Therefore the parallel currents do not close in the ionosphere, rather they partly close in the smoothing region above the ionospheric boundary. The internal ionospheric boundary conditions are set by forcing a static equilibrium at $\xi_a = 2.5\ R_E$. We reduce radius of the internal boundary from our previous simulation to more accurately simulate inner magnetospheric dynamics during strong magnetic storm events. The normalized MHD equations are solved as an initial value problem under the boundary conditions by using a modified version of the Leap-Frog method in order to obtain quasi steady state magnetospheric configuration. The simulation time step, Δt (=0.14 s), is given from the numerical stability condition of the differential scheme, $V_g^{\max}\frac{\Delta t}{\Delta x} < 1$, where $V_g^{\max}$ is the maximum group velocity in the simulation volume.

2.3 Magnetosphere-Ionosphere Relationship

The current-voltage relationship giving the interaction of the solar wind with the magnetosphere and the ionosphere was first studied by Fedder and Lyon (1987). Generally,

there are two methods to treat magnetosphere-ionosphere coupling. In the first method, the field-aligned currents (FACs), $J_\parallel$, are mapped from inner boundary of the magnetosphere to the ionosphere along magnetic field lines. The equations giving the relationship between the parallel current and the electric potential are given in (6–8) where ϕ is the electric potential, Σ is the ionospheric conductance tensor, and $J_\parallel$ is the parallel current density. Equations (6), (7), and (8) are used to calculate the velocity, $\mathbf{V}_\perp$, and electric field, $\mathbf{E}_\perp$, which are then mapped from the ionosphere back to the magnetosphere.

$$J_\parallel = \nabla \cdot \Sigma \cdot \nabla\phi \tag{6}$$

$$\mathbf{E}_\perp = -\nabla\phi \tag{7}$$

$$\mathbf{V}_\perp = \frac{\mathbf{E}_\perp \times \mathbf{B}}{B^2} \tag{8}$$

$$\mathbf{J}_\perp = \Sigma \cdot \mathbf{E}_\perp \tag{9}$$

If Σ is only the Pedersen conductivity and a constant, we have

$$\nabla^2\phi = J_\parallel \Sigma^{-1}. \tag{10}$$

Then incompressibility condition is automatically satisfied as

$$\nabla \times \mathbf{E}_\perp = 0$$

$$\nabla \cdot \mathbf{V}_\perp = 0.$$

Equation (10) shows the relationship among $J_\parallel$, Σ, and ϕ. ϕ and $\mathbf{V}_\perp$ are surely related to Σ. If Σ double for constant $J_\parallel$, ϕ and $\mathbf{V}_\perp$ should be half. Σ can be fundamentally determined by the ionospheric parameter such as the density, the temperature of the plasma, neutral gases, and the magnetic field.

In the second method, the magnetosphere and the ionosphere coupling process is handled by a reversing the procedure. Each velocity, $\mathbf{V}_\perp$, or electric field, $\mathbf{E}_\perp$ ($\mathbf{E}_\perp = -\mathbf{V}_\perp \times \mathbf{B}$), is mapped directly from the inner boundary of the magnetosphere to the ionosphere along magnetic field lines, and then the parallel current density, $J_\parallel$, is inversely mapped from the ionosphere to the magnetosphere to calculate a perturbation of the magnetic field as follows,

$$\mathbf{E}_\perp = -\mathbf{V}_\perp \times \mathbf{B} \tag{11}$$

$$J_\perp = \Sigma \cdot \mathbf{E}_\perp \tag{12}$$

$$J_\parallel = -\nabla_\perp \cdot \Sigma \cdot \mathbf{E}_\perp \tag{13}$$

If $\mathbf{E}_\perp = -\nabla\phi$ is assumed, the ionospheric potential and the parallel current density are calculated by using the relationship $\nabla^2\phi = \nabla \cdot (\mathbf{V}_\perp \times \mathbf{B})$ and $J_\parallel = \nabla \cdot \Sigma \cdot \nabla\phi$.

If a magnetic flux function, ψ, is introduced in cylindrical coordinate for simplicity, the following relation is given;

$$\mathbf{B} = \mathbf{Z} \times \nabla\psi, \tag{14}$$

where $\mathbf{Z}$ is the unit vector in Z-direction. It can be calculated from the FACs, $J_\parallel$, at the inner boundary of the magnetosphere as follows

$$\nabla^2\psi = J_\parallel. \tag{15}$$

Therefore, the magnetic field can be approximately obtained from Eq. (14).

In this case, incompressibility was not assumed in (11). Then the following conditions hold;

$$\nabla \times \mathbf{E}_\perp \neq 0$$

$$\nabla \cdot \mathbf{V}_\perp \neq 0,$$

in which the relationship of $\mathbf{E}_\perp = -\nabla\phi$ is never assumed. It is noted that the incompressibility condition is not required in the ionosphere for the second method. In this simulation, a constant Pedersen conductivity in the ionosphere is assumed to be 7 S, which is obtained from the condition that the potential peaks given by the two different methods are the same.

3. Characteristic Features of October 21–22 Events

Figure 1 shows the auroral electrojet index (top panel) and the magnetic storm disturbances index, Dst, (bottom panel) for the October 21–22, 1999, storm. During this period, the AL index had a double minimum: the first minimum of −1357 nT occurred at 0104 UT and the second minimum of −1992 nT was at 0431 UT. Dst reached a minimum value of −237 nT at 0600-0700 UT.

WIND observations of the solar wind and the IMF are shown in Fig. 2 for the period from 2300 UT on October 21 to 0800 UT on the next day. The time was shifted by 4∼6 min to account for the travel time from the WIND observation (located at $X \sim 29\ R_E$) to the Earth. The Figure shows, from top to bottom, IMF B_z, B_y, dynamic pressure (Dp), velocity (V_x), and the number density. The IMF B_z was southward (−20 to −30 nT) for ∼6 hours. The IMF B_y was dawnward until 0540 UT, when it turned duskward, reaching ∼30 nT. There were two peaks in the solar wind dynamic pressure, the second peak reached ∼52 nPa at 0716 UT. ¿From these solar wind and the IMF variations, it was expected that the strong storm event could be generated by strong southward IMF for a long duration and by increased of the solar wind dynamic pressure.

4. Simulation Results

Figure 3 shows the time evolution of the electric potential from the simulation, where $\phi(+)$, $\phi(-)$, and $\phi(+) - \phi(-)$ are the maximum, the minimum and cross polar cap potential respectively, and shaded portions of A, B and C indicate the times highlighted in Fig. 2. A few minutes after the arrival of the southward ($B_z \sim -20$ nT) from 2348 UT in the state of northward IMF, the cross polar cap potential decreases once at 2359 UT by convection reversal and then increases by nearly 240 kV. It remains nearly constant until after the second decrease in B_z (∼−30 nT) at 0316 UT. After that, it increases gradually to ∼300 kV. Lui *et al.* (2001) showed that the polar cap potential increased during and preceding the initial interval of an enhancement of

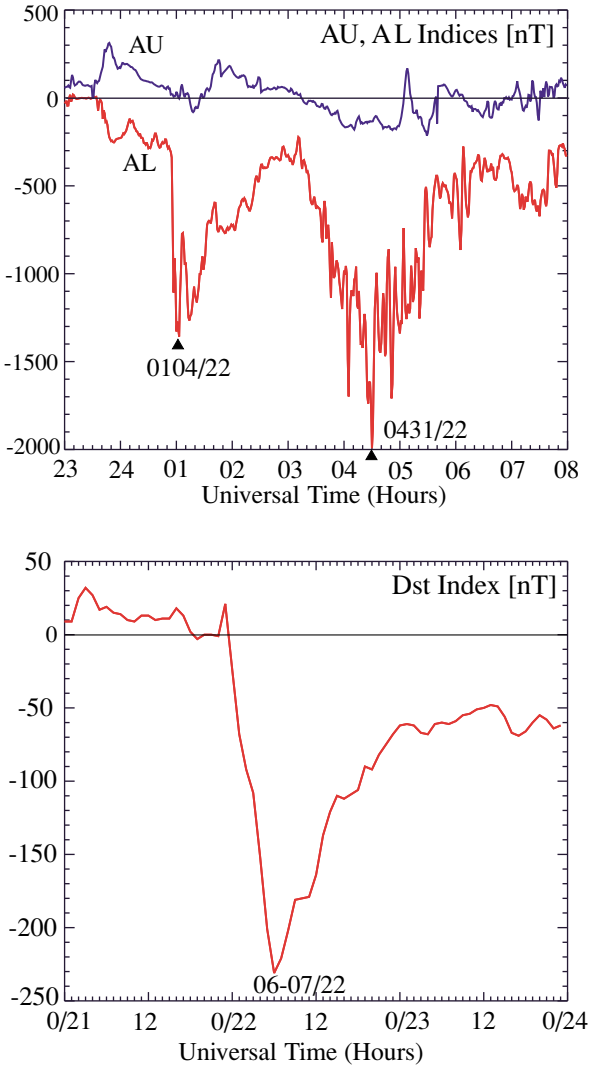

Fig. 1. Time variations of the AU, AL indices (top) and Dst index (bottom). The AL index had a minimum of −1992 nT at 0431 UT and the Dst index was a minimum of −237 nT at 0600-0700 UT.

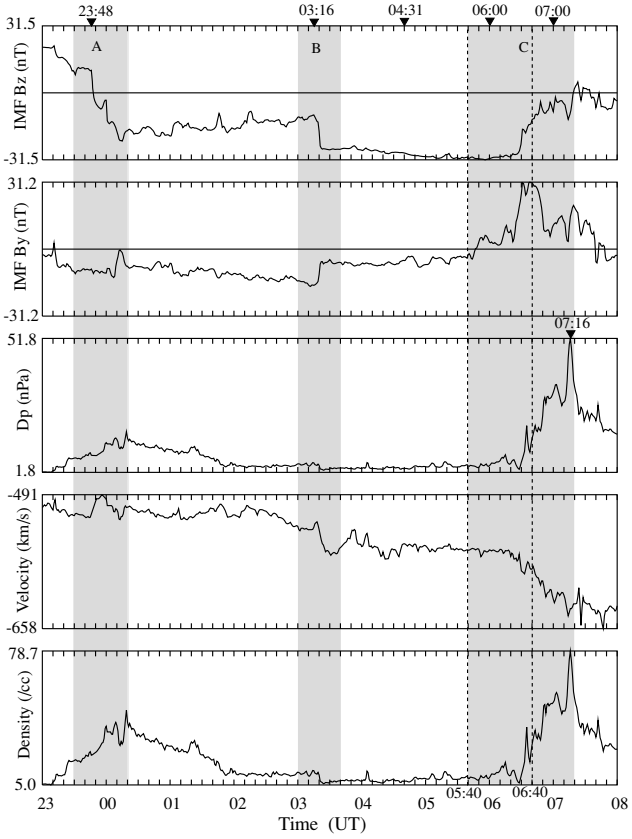

Fig. 2. WIND observations of the solar wind and the IMF from 2300 UT on October 21 to 0800 UT on October 22, 1999. From top to bottom, IMF B_z and B_y in GSM coordinates, the dynamic pressure, Dp, velocity in GSM coordinates, and the number density. A strong southward IMF ($B_z = -20$ to -30 nT) with a duration of$\sim$ 6 hours was observed during this period. Moreover, the dynamic pressure of solar wind is in the range from 1.8 to 51.8 nPa.

Energetic Neutral Atom (ENA) fluxes, indicating that enhanced convection contributes to the ring current buildup in this time. The cross polar cap potential remains to be large even though southward ($B_z \sim -8$ nT) increases at 0650 UT and then turns northward ($B_z \sim 2$ nT) at 0720 UT. The potential increases to about 330 kV at 0650 UT and then decreases to ~250 kV at 0716 UT. A spike of potential at 0720 UT is closely associated with a large spike in the solar wind dynamic pressure at 0716 UT. Note that the polar cap potential stays very high even when the IMF B_z increases and becomes northward for interval C.

Figure 4 shows the time evolution of the plasma pressure profile, P along the Sun-Earth line. The Earth is located at the origin, and the position of GEO ($\pm 6.6\ R_E$) is shown by a dotted line. Strong earthward plasma flow appears from 0018 UT in the tail and is accompanied by enhanced magnetic flux transport. The inner edge of the plasma sheet can be seen by the sharp nightside gradient in plasma pressure. It is inside of GEO during this event. Both the bow shock and the magnetopause move in response to the dynamic pressure and the IMF changes. The bow shock moves earthward to about 11.5 R_E, and the magnetopause shifts to $X = 7.2\ R_E$ from the Earth when the initial pressure waves hits the magnetosphere at 2315 UT. They again move toward the Earth when the IMF turns southward at 2348 UT. The inner edge of the plasma sheet moves to $X = -5.5\ R_E$ following the southward turning.

By 0104 UT when AL reaches −1357 nT, the bow shock approached $X = 9.7\ R_E$, while the magnetopause shifts to $X = 6.5\ R_E$, at this time the inner edge of the plasma sheet reaches up to $X = -3.2\ R_E$. Since $X = -3.2\ R_E$ is very close to the inner boundary of the simulation box, $|X| = 2.5\ R_E$, the inner edge might be much closer to the Earth in reality. At the second AL minimum (−1992 nT at 0431 UT), the bow shock moves out to $X = 14.4\ R_E$, and the magnetopause shifts to $X = 7.7\ R_E$ but the inner edge of the plasma sheet stays close to $X = -3.2\ R_E$. Finally, when the second large pressure increase reaches the Earth (between 0600 and 0700 UT), the bow shock and magnetopause move toward the Earth to $X = 8.3\ R_E$ and $X = 5.4\ R_E$, respectively. The inner edge of the plasma sheet stays close to $X = -3.2\ R_E$.

The position of the magnetopause is calculated by using the Shue's model (Shue *et al.*, 2000) and is plotted as the thick black and red ($B_z = 0$ nT) lines in Fig. 4. The red line depends only on the solar wind dynamic pressure. When

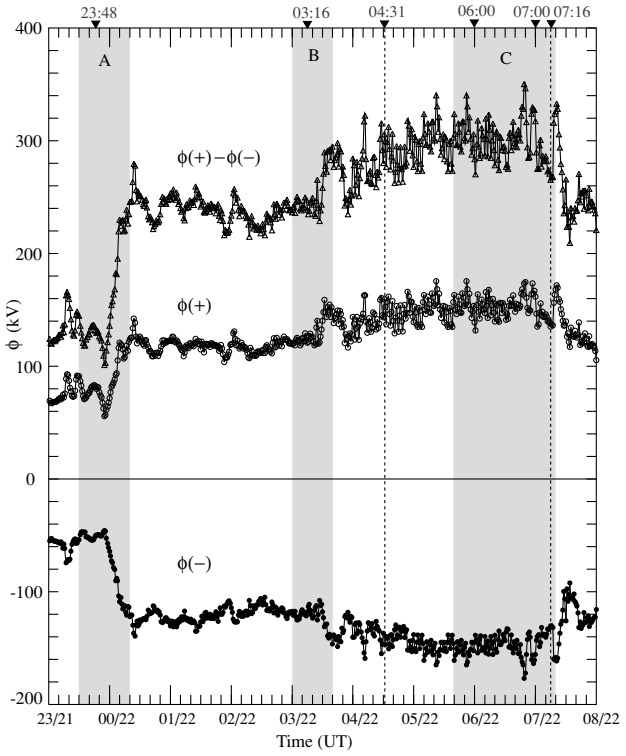

Fig. 3. Time evolution of the polar cap potential produced by the simulation. $\phi(+)$, $\phi(-)$ and $\phi(+)-\phi(-)$ are the maximum, the minimum and the cross polar cap potential respectively. The shaded portions indicate characteristic times during this storm event. The cross polar cap potential reaches $\sim$ 300 kV during the interval from 2300 UT on October 21 to 0800 UT on October 22, 1999.

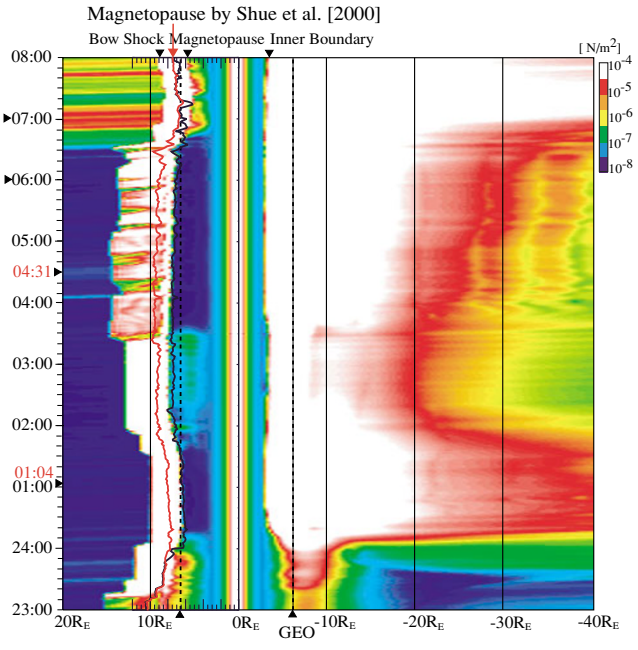

Fig. 4. Time evolution of the plasma pressure profile along the Sun-Earth line. The Earth is located at the origin, the position of GEO located at $\pm 6.6\ R_E$ is shown by dotted lines. Positions of the magnetopause by the Shue *et al.* (2000) are plotted as the thick black ($B_z \neq 0$) and red ($B_z = 0$) lines.

the IMF B_z component is non-zero, the magnetopause shifts earthward 2-3 R_E in distance in comparison with the case of

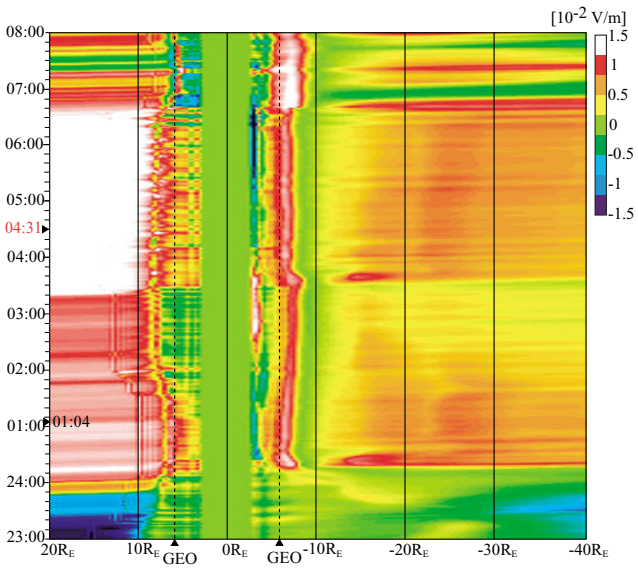

Fig. 5. Time evolution of electric field (E_y) along the Sun-Earth line. The red colors give positive or dawn to dusk electric field ($E_y > 0$) and the blue colors give negative or dusk to dawn electric field ($E_y < 0$).

zero B_z. The difference could come from the effect of the strong southward IMF. There is good agreement between the position of the simulated magnetopause and that of the Shue's magnetopause model (black line). However, the position of the simulated magnetopause shifts more earthward after 0640 UT. This additional erosion is attributable to the dayside reconnection for the strong IMF B_y component.

Figure 5 shows the time evolution of the electric field, $E_y = V_x \times B_z$, on the Sun-Earth line from 2300 UT on October 21 to 0800 UT on October 22. The red color indicates positive values of E_y (dawn to dusk) and the blue color indicates negative values. A near-Earth neutral line (NENL) appears around $X = -10\ R_E$ as a gap between two enhanced regions of E_y in the tail. A high dawn to dusk electric field appears after 0015 UT on the nightside because of the strong southward IMF ($B_z = -23$ nT at 0015 UT). This is 49 minutes before the time when the first electrojet minimum is reached at 0104 UT. The duskward electric field is enhanced at 0335 UT and penetrates inside GEO after the arrival of a more southward IMF B_z at 0316 UT. Then 51 minutes later, the second electrojet minimum occurs (-1992 nT at 0431 UT). E_y becomes very large at 0640 UT on the nightside, in response to the IMF B_z minimum (-31 nT) at 0556 UT. Dst reaches its minimum value of -237 nT between 0600 and 0700 UT and the IMF B_y is maximum (31 nT) at 0631 UT. The high duskward electric field, E_y, is maintained on the nightside even though IMF B_z has near zero value. IMF B_y is duskward with a large value of 21 nT at 0718 UT.

When E_y is 6.5×10^{-3} V/m ($V_x = -466$ km/s, $B_z = -14$ nT) in the solar wind at 0104 UT, the convective electric field becomes comparable to the solar wind electric field for $-10\ R_E < X < -3\ R_E$ in the Earth-side region (inner plasma sheet) of NENL; it is 37% of solar wind electric field for $X < -10\ R_E$ in the tail-side region (outer plasma sheet). It becomes over 50% in the inner plasma sheet and

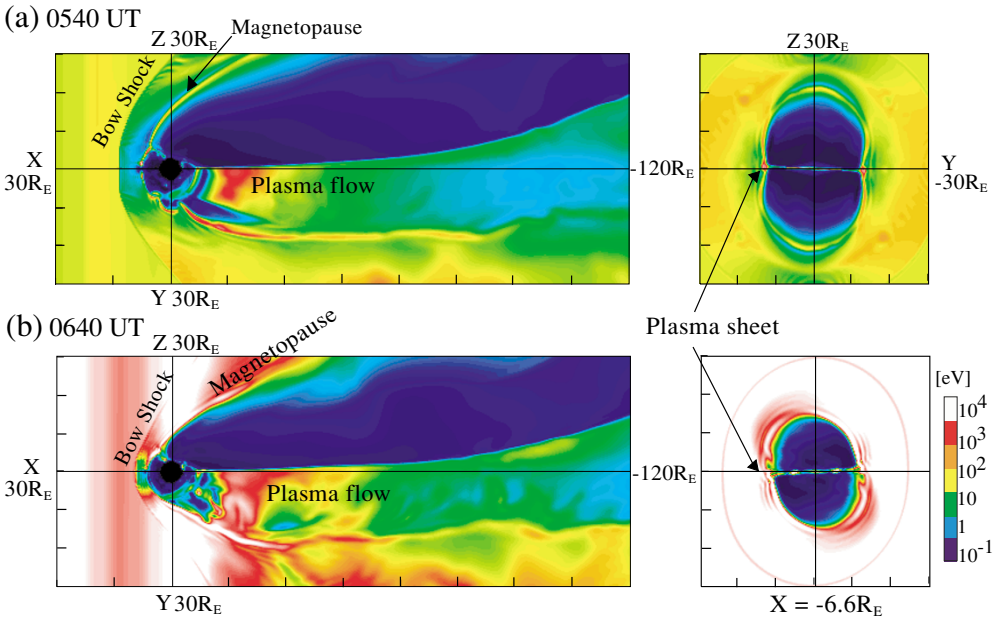

Fig. 6. Simulation results showing the kinetic energy at 0540 UT (top panel) and at 0640 UT (bottom panel). On the left, the upper (lower) half shows the simulation results in $XZ(XY)$ plane. The right hand panels are cross sections of the plasma sheet at $X = -6.6\ R_E$.

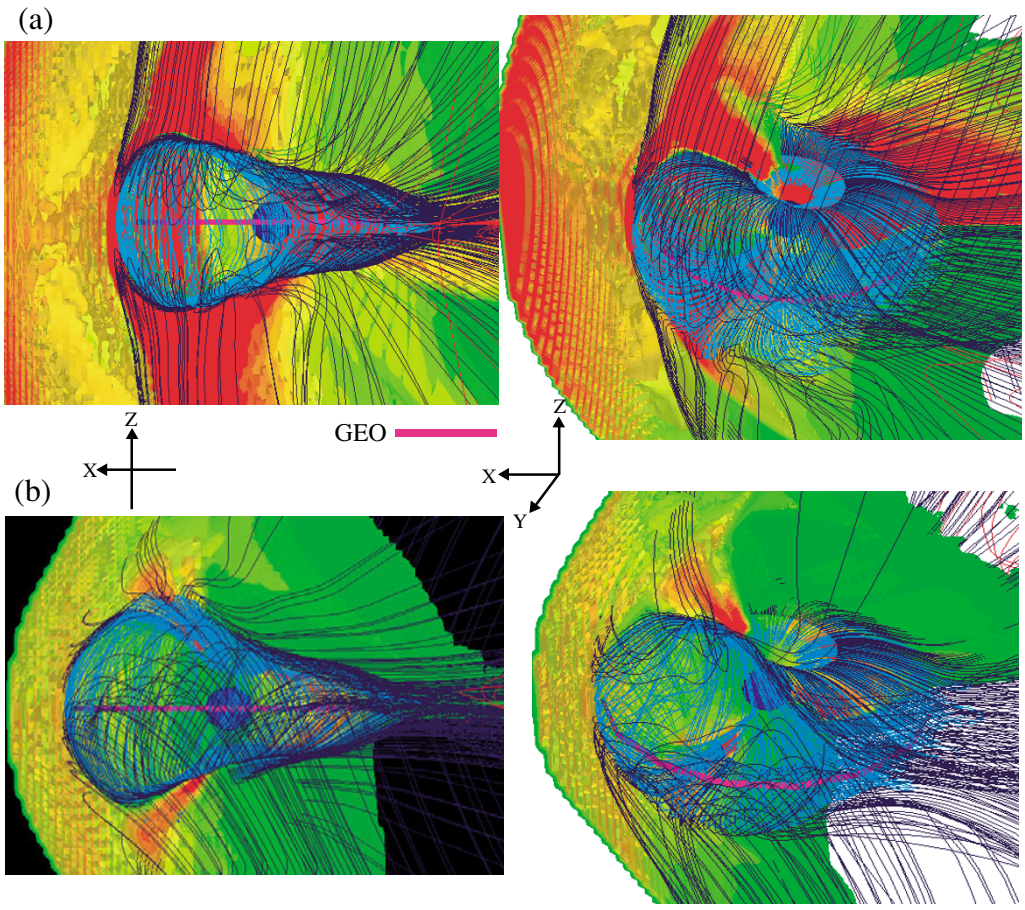

Fig. 7. Configuration of the magnetic field line and the plasma temperature from the MHD simulation at 0540 UT (top panels) and 0640 UT (bottom panels) shown from duskside (left) and tail-duskside (right). Closed field lines that connect to the Earth in both directions are blue; open field lines that connect to the ionosphere at one end and to the distant IMF at the other are dark blue. Red field lines are not connected to the Earth at all. The plasma temperature is shown by three-dimensional iso-surface only on the dawnside, and the color scale shows green-yellow-red going from low to high temperatures.

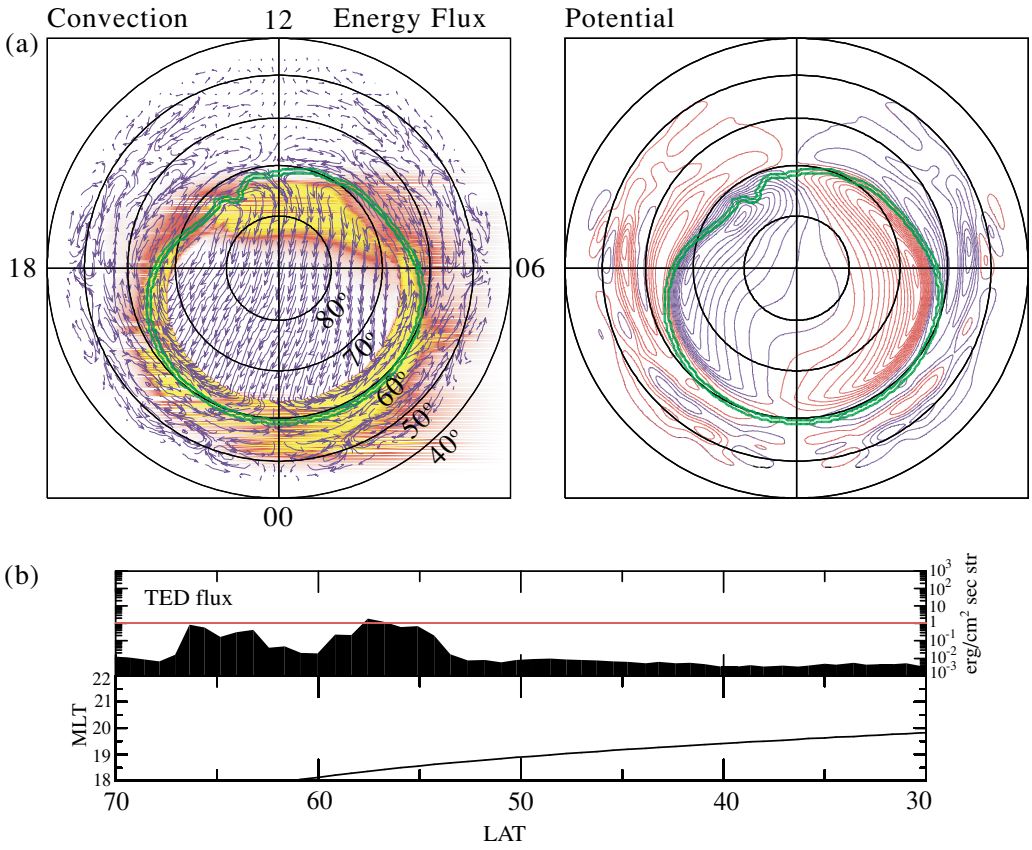

Fig. 8. (a) (left) Convection pattern and energy flux, and (right) polar-cap potential mapped onto the ionosphere obtained by the MHD simulation. The bottom panel (b) is the downward electron energy flux at energies of 0.02−20 keV observed by the TED instrument from the NOAA-15 satellite.

is almost 20% in the outer plasma sheet while the IMF B_z is strongly southward for 0330−0540 UT. At 0600−0800 UT, E_y increases between 90% and 200% in the inner plasma sheet due to compression caused by the strong increase of the solar wind dynamic pressure. Thus a convective electric field, which is almost comparable to (or over) that of the solar wind, can penetrate in to the Earth-side of NENL.

Figure 6 shows the kinetic energy ($K = \frac{1}{2}\rho V^2$) from the simulation (a) at 0540 UT and (b) at 0640 UT. In the left panel, the values in the noon-midnight meridian are plotted on the upper half (XZ) while equatorial values are found on the lower half (XY). The right hand panels are cross sections of the plasma sheet at $X = -6.6\ R_E$. We see the locations of the bow shock and the magnetopause in the kinetic energy at the dayside magnetosphere. In the top left the panel, stream-like structure of higher kinetic energy (just below the magnetopause) extends from the cusp toward the mantle. The panel also shows strong tailward plasma flow in the plasma sheet. In the bottom panel (0640 UT), the bow shock and the magnetopause are located closer to the Earth than in the top panel, the whole magnetosphere is compressed by a strong increase of solar wind dynamic pressure. A large amount of the plasma flows tailward over a wide region of the plasma sheet.

Figure 7 shows a three-dimensional view of the magnetosphere at two characteristic times. The configuration of the magnetic field lines and the plasma temperature is shown at 0540 UT (a) and 0640 UT (b). The plasma temperature is shown by 3-D iso-surface only on the dawnside and the color scale is green-yellow-red going from low to high temperature. Closed field lines that connect to the Earth in both ends are blue, open field lines that connect to the ionosphere at one end and to the distant IMF at the other are dark blue, and detached field lines (IMF) that do not connect to the Earth at all are red. As shown in Fig. 2, at 0540 UT, the IMF is strongly southward with a smaller dawnward B_y component ($B_z = -31$ nT and $B_y = -1.7$ nT). At 0640 UT, the IMF B_z is one-third of its former value, and there is a large duskward B_y component ($B_z = -12$ nT and $B_y = 31$ nT). The dayside reconnection can be seen at $X = 7.5\ R_E$, and tail reconnection can be found at $X = -8.8\ R_E$ in Fig. 7(a). The dayside reconnection occurs near the GEO region at high-latitudes and tail reconnection is about $X = -10\ R_E$ in Fig. 7(b). The region is verified from the B_z profile along Sun-Earth line. It should be noted that a sharp transition from dipole-like to tail-like magnetospheric configurations occurs near the GEO region in the tail.

Figure 8(a) shows the ionospheric convection/energy flux and the potential mapped onto the polar region. The physical quantities are mapped onto the ionosphere along the magnetic field lines by using $\int \frac{f}{B} dl / \int \frac{1}{B} dl$, where f stands for each of the physical quantities and B is the magnitude of magnetic field. Figure 8(b) shows the observation of the energetic electron data from the NOAA-15. Bottom panel is the downward electron energy flux from 20 eV to 20 keV from the TED instrument. Details of Total Energy Detec-

Table 1. Response of the Earth's magnetosphere to variations of the solar wind and the IMF. Where BS means the bow shock, MP the magnetopause, PS the inner boundary of plasma sheet, PCP the cross polar cap potential and Dp the dynamic pressure.

Time (UT)		Observation	Simulation results
	2300		Northward IMF B_z, Four-cell convection pattern
↑	2348	IMF B_z turns N→S	BS: 11.5 R_E, MP: 7.2 R_E, PS: −5.5 R_E
	2355		Two-cell convection pattern, PCP minimum
	0010		PCP increase ∼250 kV (to 0330 UT)
A	0012		Onset of tail reconnection
	0015		Duskward E_y increases (7.3 R_E)
↓	0018		Fast plasma flow in tail, BS: 9.5 R_E, MP: 6.4 R_E, PS: −5.2 R_E
	0040		PS appears ∼3 R_E
	0104	AL minimum (−1357 nT)	
↑	0316	IMF $B_z = -20$ nT→−30 nT	BS: 12.5 R_E, MP: 7.8 R_E. PS: −3.2 R_E
B	0326		BS moves out 11.4 R_E (to 6:30 UT)
↓	0335		Duskward E_y increase
	0431	AL minimum (-1992 nT)	BS: 14.4 R_E, MP: 7.7 R_E, PS: −3.2 R_E
↑	0546	IMF B_y dusk → dawn	
	0556	IMF $B_z = -31.5$ nT	
	0600	Dst = −237 nT (6–7 UT), Dusk proton flux ($L = 3$)	BS: 8.3 R_E, MP: 5.4 R_E, PS: −3.2 R_E
C	0631	IMF $B_y = 31.2$ nT	
	0640		PCP reaches ∼300 kV, Energy flux extends at 50° latitude, Duskward E_y increases (7.6 R_E)
	0716	$Dp = 51.8$ nPa	
↓	0720		Duskward E_y increases (7.3 R_E)

tor (TED) and Medium Energy Proton and Electron Detector (MEPED) are described in Evans and Greer (2000). It should be noted that 1 erg/cm^2 sec str could be proxy for visible aurora (Yahnin *et al*., 1997). By 0640 UT, the cross polar cap potential is already increased (Fig. 3), indicating that the convection is enhanced in the ionosphere.

The flow in the throat region (near noon) is poleward on the dayside in the top left panel, and the region of enhanced energy flux on the dayside is confined in the cusp region. Enhanced nightside energy flux extends as low as 50° latitude in simulation. At 19 magnetic local time (MLT), the energy flux appears at 55° latitude in simulation (Fig. 8(a)), consistent with the low latitude, 52° of the TED in observation of the NOAA-15 (Fig. 8(b)). On the right of Fig. 8(a), the red contour indicates positive potential and blue contour indicates negative potential. The positive potential peak moves tailward in comparison with negative potential due to the large positive B_y component. The green lines delimit the open-closed field boundary. The open-closed boundary extends at 60° on the nightside, 72° on the dayside, 62° on dawn, and 66° on dusk. The 66° latitude of the open-closed boundary at 17 MLT is consistent with the high-latitude boundary of the TED flux enhancement region, which should correspond to the high-latitude boundary of the auroral oval.

5. Chronology of the Magnetic Storm

We divide these simulation results into three characteristic time intervals: when B_z turns from northward to southward, when B_z becomes more southward, and when B_z turns from southward to northward. The three characteristic intervals correspond to the shaded portions of A, B, and C in Figs. 2 and 3. The storm event timings are summarized in Table 1.

5.1 Interval A: IMF B_z turns from northward to southward (2330-0020 UT)

When the IMF turns from northward to southward at 2348 UT, the initial four-cell convection pattern in the polar ionosphere gradually changes to a two-cell convection pattern. The cross polar cap potential increases up to 300 kV and the convective flow increases on the dayside. Fast plasma flow is generated in the plasma sheet just 6 minutes after the onset of tail reconnection at 0018 UT. In this time, the Alfvén Mach number, $M_A = V_{sw}/V_A = 8.47$, and the bow shock moves to $X = 9.5\ R_E$, while the magnetopause shifts to $X = 6.4\ R_E$ and the inner edge of the plasma sheet moves to the Earth to $X = -5.2\ R_E$.

5.2 Interval B: IMF B_z becomes more southward (0300-0340 UT)

When the IMF B_z becomes more southward from −11 to −26.8 nT at 0316 UT, E_y increases on the nightside at 0335 UT; in addition, the cross polar cap potential increases from 250 to 300 kV. The energy flux in the ionosphere de-

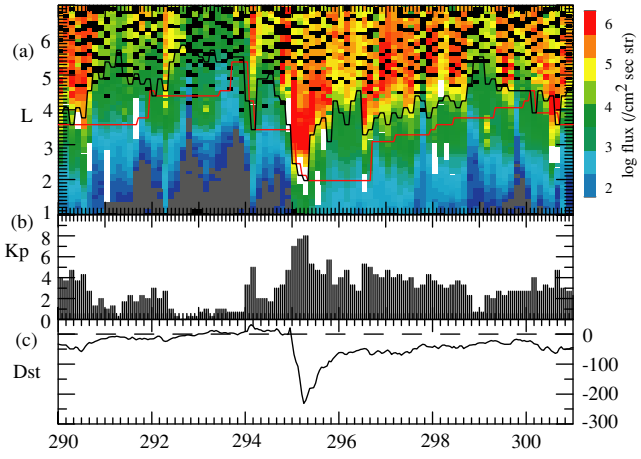

Fig. 9. (a) L value with time diagram for the proton flux, represented by the color code.The trapped proton flux is observed in the duskside. The red line is location of the plasmapause, while the black line is the reference line to represent the variation of the convection limit. (b) Kp and (c) Dst indices are represented on the lower two panels.

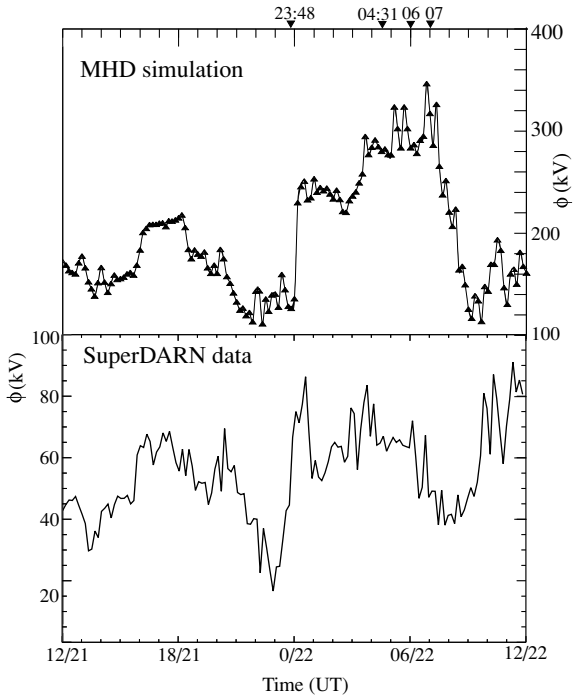

Fig. 10. Comparison between the cross polar cap potential pattern from the MHD simulation and that inferred from the SuperDARN observations.

creases in the dayside region because the dynamic pressure of the solar wind decreases. Due to the effect of the decreases in pressure and the low Mach number ($M_A = 2.42$), the bow shock moves out to $X = 14.4\ R_E$, while the magnetopause shifts to $X = 7.7\ R_E$ and the inner edge of the plasma sheet close to $X = -3.2\ R_E$.

5.3 Interval C: IMF B_z turns from southward to northward (0540−0720 UT)

During this interval, IMF B_z is still strongly southward ($\sim$−30 nT) until 0630 UT, and then IMF B_z becomes more northward. The IMF B_y is a large positive value and the dynamic pressure increases, the energy flux in the ionosphere increases on the dayside and the cross polar cap potential remains constant at a high value of 300 kV. The duskward electric field increases on the nightside from 0640 UT. The bow shock approaches to $X = 8.3\ R_E$, while the magnetopause shifts to $X = 5.4\ R_E$ and the inner edge of the plasma sheet stays at $X = -3.2\ R_E$.

6. Discussion

In this paper, we have studied the response of the Earth's magnetosphere to variations in the solar wind and the IMF. The strong magnetic storm event of October 21 and 22 could be well represented even in the near-Earth magnetotail region by this simulation.

The cross polar cap potential increases and reaches a maximum at 0010 UT, 16 minutes after the IMF turns from northward to southward. The response of the magnetosphere takes a short time from variations of the solar wind. The time is considered to be 4–6 min to allow for the propagation of the solar wind from the WIND position to the Earth. Note that the substorm occurs in the tail accompanied with a strong earthward flow, caused by the enhanced convection (duskward E_y increases) due to the tail reconnection.

Figure 9 shows the L value-time spectrogram for 30–80 keV proton flux from the MEPED instrument the NOAA-15. This energy has been considered as the main part of ring current. The trapped proton flux observed in the dusk side is in panel (a). The Kp (b) and Dst (c) indices are represented on the lower two panels. The red line is the location of the plasmapause evaluated from the empirical relation as a function of the Kp index by O'Brien and Moldwin (2003). The black is also derived from the same relationship, but the refilling time of plasmasphere is not considered. Thus, it is supposed that the black line can be a proxy for activity of magnetospheric convection. The proton flux enhancement is observed when the magnetic storm at lower L value, $L < 3$, in the NOAA-15 data. This implies that the inner boundary of the plasma sheet moves toward the Earth concurrently with the convection enhancement, and such movement of the plasma sheet can be clearly seen in our simulation (cf. Fig. 4).

We also have compared our simulation results of the polar cap potential with the SuperDARN observations in Fig. 10. The simulated cross polar cap potential is $\sim$3−4 times larger than that inferred from the SuperDARN observations. However the characteristic timings of the increase and decrease in the potential are similar from 1200−2100 UT on October 21. The second method in Section 2.3 that we use to obtain the polar cap potential, in principle, does not depend on the ionospheric conductivity because the feedback effect is neglected. It is noted that the cross polar cap potential obtained gives the maximum generated by the inner magnetospheric convection. Therefore, the polar cap potential in reality can be less than that given in the present simulation. The polar cap potential depends on the ionospheric conductivity due to the feedback effect. The difference of magnitude of the polar cap potential needs further study comparing the two methods to give the magnetosphere-ionosphere relationship.

Both the cross polar cap potential in the simulation and

the SuperDARN observation increased just after the IMF B_z turned from northward to southward at 2348 UT. The simulated cross polar cap potential reached 300 kV, whereas the SuperDARN observations give only about 68 kV. The polar cap potential in simulation is almost constant with 250 kV during the strong southward IMF B_z (-20 nT) for 3 hours at 0100-0300 UT. Then it increases from 250 to 300 kV when the IMF B_z is more southward from -20 to -30 nT at 0300-0600 UT. The time variation is similar to that of the PC index (e.g., Troshichev *et al*., 1996). On the other hand, the potential shown from SuperDARN observations quickly decreases from 0015 UT on October 22 and then it did not increase so strongly at 0300−0600 UT on October 22. This result comes from the increased ionospheric conductivity due to the enhanced of the magnetospheric convection and the field-aligned currents. The dense particle precipitation in the nightside (e.g., DMSP data) leads to the increase in ionospheric conductivity, and the potential is sensitive to the conductance (Richmond *et al*., 1988; Richmond, 1992). Thus the polar cap potential of the SuperDARN quickly decreases. Moreover, the SuperDARN potential is not so much increased for the strong southward IMF B_z (~ -30 nT), partly because of insufficient data coverage during the strong magnetic storm period.

The cross polar cap potential saturates for a strong B_z component. Siscoe *et al*. (2002) proposed that the saturation of the polar cap potential originated from the ionospheric conductivity and region 1 current limitation by ram pressure. Merkine *et al*. (2003) showed, by using global MHD modeling, that the potential saturated as the solar wind electric field increased, and that the saturation level was strongly affected by the ionospheric conductance. However, the saturation mechanism (Interval B) in this event study is independent of the ionospheric conductivity, suggesting another possibility of the saturation mechanism. The mechanism may be connected to a relative reduction of the dayside magnetic reconnection rate. We find in our simulation that the reconnected open field lines at the dayside magnetopause is almost parallel to the IMF. The reconnected field line are not fully carried away from the reconnection region due to very strong southward IMF and normal solar wind speed. Therefore, the reconnection rate does not remarkably increase even though IMF B_z decreases down to -30 nT.

The cross polar cap potential in the simulation is maintained at a large value even when the IMF B_z becomes less negative or even positive. This is caused by the large IMF B_y at this time (Fig. 2), and the IMF lines can directly approach reconnection regions at the dayside magnetopause close to the Earth. The dayside reconnection occurs at high latitudes in the northern dusk sector close to the GEO with naked geomagnetic field lines because of the large duskward IMF B_y component at 0640 UT. Therefore, the convection enhancement in the ionosphere appears and leads to a large value of the cross polar cap potential.

7. Conclusions

We have used a three-dimensional global MHD model to simulate the interaction of the solar wind with the Earth's magnetosphere to study a strong magnetic storm on October 21–22, 1999, when the IMF was strongly southward ($B_z = -20$ to -30 nT) for $\sim$6 hours. The dynamic pressure of the solar wind was in the range 1.8−51.8 nPa during this period. The simulation reproduced the time evolution of the cross polar cap potential, the kinetic energy, the plasma pressure, E_y, and the locations of the bow shock, the magnetopause, and the inner edge of plasma sheet in this event.

The following conclusions can be obtained from the present simulation:

1) As the IMF is strongly southward (-20 nT to -30 nT) for 6 hours, the geomagnetic field lines in the dayside magnetopause are eroded to the GEO region by reconnection. Moreover, the associated magnetic flux is transferred from the dayside magnetosphere to the tail. Reconnection still occurs near the GEO region on the dayside magnetopause (Fig. 7(b)), even though the IMF B_z component becomes small or even turns to northward, because of the influence of the following a strong IMF B_y (30 nT). During the large B_y interval, the IMF lines can reconnect the naked geomagnetic field with a large magnitude in the high-latitude flanks. Thus the cross polar cap potential is maintained at a large value and the convection in the ionosphere is enhanced. The cross polar cap potential is governed by IMF B_y as well as B_z components. It saturates for the strong southward IMF ($\phi \sim 250$ kV for $B_z \sim -20$ nT and $\phi \sim 300$ kV for $B_z \sim -30$ nT). Potential saturation may be connected to relative reduction of the dayside magnetic reconnection rate. We find in our simulation that the reconnected open field lines at the dayside magnetopause are almost parallel to the IMF. The reconnected field lines are not fully carried away from the reconnection region for very strong southward IMF and normal solar wind speed. Therefore, the reconnection rate does not increase remarkably, even though IMF B_z decreases down to -30 nT.
2) The dynamic pressure of the solar wind shows a spiky peak for a short interval (about 10 minutes), however it has a rather small effect on the cross polar cap potential increases as both the absolute values of IMF B_y and IMF B_z are gradually decreasing at that time. Enhanced energy flux appears at low latitude (50°) on the nightside in simulation. The energy flux in the region 19 MLT, appears down to a 55° latitude in simulation and is consistent with the low latitudes, 52° of the energetic electrons from the NOAA-15 satellite. The open-closed boundary extends to lower latitudes at 60° on the nightside, 72° on the dayside, 62° on dawn, and 66° on dusk. The 66° latitude on dusk from the simulation is consistent with the high-latitude boundary of TED flux enhancement region.
3) The initial plasma pressure change leads to a strong earthward flow at 0040 UT in the simulation. This is the start of a substorm and is consistent with the decrease in the AL index, corresponding to the development of auroral electrojet current (Fig. 1).
4) During the storm main phase, the bow shock approaches $X = 8.3\ R_E$, while the magnetopause shifts to $X = 5.4\ R_E$ and the inner edge of the plasma sheet

close to $-3.2\ R_E$ at the time when the dynamic pressure of the solar wind reaches its maximum value at ~0700 UT. At the same time, E_y increases by 90–200% in the inner plasma sheet due to compression by the strong increase of the solar wind dynamic pressure. The convective electric field, which is almost comparable to (or larger than) that of the solar wind, penetrates into the Earth-side of NENL.

We have obtained the magnetospheric configuration and dynamics for a event study of a strong magnetic storm. The large energy flux enters the ionosphere at very low latitudes and the inner edge of the plasma sheet becomes very close to the Earth for a strong magnetic storm. These results are consistent with the observation data. The present MHD simulation study gave reasonable results in near-Earth magnetotail dynamics even for extreme conditions and thereby its usefulness could be demonstrated as a physical model for space weather studies.

Acknowledgments. We would like to thank Raymond J. Walker, Hiroyuki Shinagawa, Yoshizumi Miyoshi, Yukinaga Miyashita and Kazuo Shiokawa for helpful discussions A. T. Y. Lui for providing the polar cap potential data and Nozomu Nishitani for useful discussion on the potential maps from the SuperDARN radars in the northern hemisphere. The WIND data of solar wind and magnetic field in ISTP Key Parameters were provided courtesy of Drs. K. W. Ogilvie and R. P. Lepping respectively. The geomagnetic indices AL, AU and Dst were provided by the WDC for Geomagnetism in Kyoto. The data from the NOAA satellites were provided by NOAA through the WDC-C2 for Aurora, National Institute of Polar Research, Japan. Computing support was provided by the Information Technology Center of Nagoya University. Support was provided by Grants-in-Aid from the Japan Society for Promotion of Science (JSPS).

References

Ashour-Abdalla, M., M. El-Alaoui, V. Peroomian, R. J. Walker, L. M. Zelenyi, L. A. Frank, and W. R. Paterson, Localized reconnection and substorm onset on Dec. 22, 1996, *Geophys. Res. Lett.*, **26**, 3545–3548, 1999.

Ashour-Abdalla, M., M. El-Alaoui, F. V. Coroniti, R. J. Walker, and V. Peroomian, A new convection state at substorm onset: Results from an MHD study, *Geophys. Res. Lett.*, **29**, 1965, 2002a.

Ashour-Abdalla, M., M. El-Alaoui, V. Peroomian, R. J. Walker, L. M. Zelenyi, L. A. Frank, and W. R. Paterson, The origin of the near-Earth plasma population during a substorm on November 24, 1996, *J. Geophys. Res.*, **105**, 2589–2605, 2002b.

Brecht, S. H., J. G. Lyon., J. A. Fedder, and K. Hain, A simulation study of east-west IMF effects on the magnetosphere, *Geophys. Res. Lett.*, **8**, 397–400, 1981.

Evans, D. S. and M. S. Greer, Polar orbiting environmental satellite space environment monitor: 2. Instrument description and archive data documentation, *NOAA Tech. Memo. OAR SEC-93*, *Natl. Oceanic and Atmos. Admin., Boulder, Colo.*, 2000.

Fedder, J. A. and J. G. Lyon, The solar wind-magnetosphere-ionosphere current-voltage relationship, *Geophys. Res. Lett.*, **14**, 880–883, 1987.

Fedder, J. A., S. P. Slinker, J. G. Lyon., and R. D. Elphinstorne, Global numerical simulation of the growth phase and the expansion onset for a substorm observed by Viking, *J. Geophys. Res.*, **100**, 19083–19093, 1995.

Le, G., J. Raeder, C. T. Russell, G. Lu, S. M. Petrinec, and F. S. Mozer, Polar cusp and vicinity under strongly northward interplanetary magnetic field on April 11, 1997: Observations and MHD simulations, *J. Geophys. Res.*, **106**, 21083–21093, 2001.

Lui, A. T. Y., R. W. McEntire, and K. B. Baker, A new insight on the cause of magnetic storms, *Geophys. Res. Lett.*, **28**, 3413–3416, 2001.

Lyon, J. G., S. H. Brecht, J. D. Huba, J. A. Fedder, and P. J. Palmadesso, Computer simulation of a geomagnetic substorm, *Phys. Rev. Lett.*, **46**, 1038–1041, 1981.

Lyons, L. R., The Geospace Modeling Program Grand Challenge, *J. Geophys. Res.*, **103**, 14781–14785, 1998.

Lyons, L. R., J. M. Ruohoniemi, and G. Lu, Substorm-associated changes in large-scale convection during the November 24, 1996, Geospace Environment Modeling event, *J. Geophys. Res.*, **106**, 397–405, 2001.

Merkine, V. G., K. Papadopoulos, G. Milikh, A. S. Sharma, X. Shao, J. Lyon, and G. Goodrich, Effects of the solar wind electric field and ionospheric conductance on the cross polar cap potential: Results of global MHD modeling, *Geophys. Res. Lett.*, **23**, 2180, 2003.

O'Brien, T. P. and M. B. Moldwin, Empirical plasmapause models from magnetic indices, *Geophys. Res. Lett.*, **30**, 1152, 2003.

Ogino, T., R. J. Walker, M. Ashour-Abdalla, and J. M. Dawson, An MHD simulation of B_y-dependent magnetospheric convection and field-aligned currents during northward IMF, *J. Geophys. Res.*, **90**, 10835–10842, 1985.

Ogino, T., R. J. Walker, and M. Ashour-Abdalla, A global magnetohydrodynamic simulation of the magnetosheath and magnetosphere when the interplanetary magnetic field is northwards, *IEEE Trans. Plasma Sci.*, **20**(6), 817, 1992.

Raeder, J., J. Berchem, and M. Ashour-Abdalla, The Geospace Environment Modeling Grand Challenge: Results from a global geospace circulation model, *J. Geophys. Res.*, **103**, 14787–14797, 1998.

Raeder, J., R. L. McPherron, L. A. Frank, S. Kokubun, G. Lu, T. Mukai, W. R. Paterson, J. B. Sigwarth, H. J. Singer, and J. A. Slavin, Global simulation of the Geospace Environment Modeling substorm challenge event, *J. Geophys. Res.*, **106**, 381–395, 2001.

Richmond, A. D., Y. Kamide, B.-H. Ahn, S.-I. Akasofu, D. Alcayde, M. Blanc, O. de la Beaujardiere, D. S. Evans, J. C. Foster, E. Friis-Christensen, T. J. Fuller-Rowell, J. M. Holt, D. Knipp, H. W. Kroehl, R. P. Lepping, R. J. Pellinen, C. Senior, and A. N. Zaitzev, Mapping electrodynamic features of the high-latitude ionosphere from localized observations: Combined incoherent-scatter radar and magnetometer measurements for January 18–19, 1984, *J. Geophys. Res.*, **93**, 5760–5776, 1988.

Richmond, A. D., Assimilative mapping of ionospheric electrodynamics, *Adv. Space Res.*, **12**, 59–68, 1992.

Shue, J.-H., P. Song, C. T. Russell, J. K. Chao, and Y.-H. Yang, Toward predicting the position of the magnetopause within geosynchronous orbit, *J. Geophys. Res.*, **105**, 2641–2656, 2000.

Siscoe, G. L., N. M. Crooker, and K. D. Siebert, Transpolar potential saturation: Role of region 1 current system and solar wind ram pressure, *J. Geophys. Res.*, **107**, 1321–1328, 2002.

Slinker, S. P., J. A. Fedder, J. M. Ruohoniemi, and J. G. Lyon, Global MHD simulation of the magnetosphere for November 24, 1996, *J. Geophys. Res.*, **106**, 361–380, 2001.

Troshichev, O., H. Hayakawa, A. Matsuoka, T. Mukai, and K. Tsuruda, Cross polar cap diameter and voltage as a function of PC index and interplanetary quantities, *J. Geophys. Res.*, **101**, 13429–13435, 1996.

Walker, R. J., T. Ogino, J. Raeder, and M. Ashour-Abdalla, A global magnetohydrodynamic simulation of the magnetosphere when the interplanetary magnetic field is southward: the onset of magnetotail reconnection, *J. Geophys. Res.*, **98**, 17235–17246, 1993.

Watanabe, K. and T. Sato, Global simulation of the solar wind-magnetosphere interaction: The importance of its numerical validity, *J. Geophys. Res.*, **95**, 75–88, 1990.

Yahnin, A. G., V. A. Sergeev, B. B. Gvozdenvsky, and S. Vennerstrom, Magnetospheric source region of discrete auroras inferred from their relationship with isotropy boundaries of energetic particles, *Ann. Geophys.*, **15**, 943–958, 1997.

K. S. Park (e-mail: sun@stelab.nagoya-u.ac.jp) and T. Ogino